Disrupted osteocyte connectivity and pericellular fluid flow in bone with aging and defective TGF-β signaling

Charles A. Schurman[a,b], Stefaan W. Verbruggen[c,d,e,f], and Tamara Alliston[a,b,1]

[a]Department of Orthopaedic Surgery, University of California, San Francisco, CA 94143; [b]UC Berkeley-UCSF Graduate Program in Bioengineering, San Francisco, CA 94143; [c]Institute of Bioengineering, School of Engineering and Materials Science, Queen Mary University of London, London, United Kingdom, E1 4NS; [d]Department of Mechanical Engineering, University of Sheffield, Sheffield, United Kingdom, S1 3JD; [e]The Insigneo Institute for In Silico Medicine, University of Sheffield, Sheffield, United Kingdom, S1 3JD; and [f]Department of Biomedical Engineering, Columbia University in the City of New York, New York, NY 10027

Edited by Mitchell B. Schaffler, New York City College of Technology, New York, NY, and accepted by Editorial Board Member Lia Addadi May 11, 2021 (received for review November 24, 2020)

Skeletal fragility in the elderly does not simply result from a loss of bone mass. However, the mechanisms underlying the concurrent decline in bone mass, quality, and mechanosensitivity with age remain unclear. The important role of osteocytes in these processes and the age-related degeneration of the intricate lacunocanalicular network (LCN) in which osteocytes reside point to a primary role for osteocytes in bone aging. Since LCN complexity severely limits experimental dissection of these mechanisms in vivo, we used two in silico approaches to test the hypothesis that LCN degeneration, due to aging or an osteocyte-intrinsic defect in transforming growth factor beta (TGF-β) signaling (TβRII$^{ocy-/-}$), is sufficient to compromise essential osteocyte responsibilities of mass transport and exposure to mechanical stimuli. Using reconstructed confocal images of bone with fluorescently labeled osteocytes, we found that osteocytes from aged and TβRII$^{ocy-/-}$ mice had 33 to 45% fewer, and more tortuous, canaliculi. Connectomic network analysis revealed that diminished canalicular density is sufficient to impair diffusion even with intact osteocyte numbers and overall LCN architecture. Computational fluid dynamics predicts that the corresponding drop in shear stress experienced by aged or TβRII$^{ocy-/-}$ osteocytes is highly sensitive to canalicular surface area but not tortuosity. Simulated expansion of the osteocyte pericellular space to mimic osteocyte perilacunar/canalicular remodeling restored predicted shear stress for aged osteocytes to young levels. Overall, these models show how loss of LCN volume through LCN pruning may lead to impaired fluid dynamics and osteocyte exposure to mechanostimulation. Furthermore, osteocytes emerge as targets of age-related therapeutic efforts to restore bone health and function.

aging | osteocytes | lacunocanalicular network | transforming growth factor beta | osteocyte osteolysis

Age-related bone fragility results from the concomitant decline of bone mass and bone quality over a lifetime. Deregulation of osteoclast and osteoblast function with age contributes directly to this bone fragility, especially the loss of bone mass (1, 2). Although osteocytes comprise 90 to 95% of all bone cells, relatively little is known about their role in the age-related decline in bone health. Osteocytes reside within the bone matrix in a series of cavities and channels known as the lacunocanalicular network (LCN) (3, 4). Within the LCN, osteocytes act as master regulators of bone health by supplying nutrients to other osteocytes distal to the vasculature by coordinating the activity of osteoblasts, osteoclasts, and other cell types to balance bone deposition and resorption (5, 6) by sensing and responding to mechanical forces (7) and by actively remodeling their surrounding bone matrix via perilacunar/canalicular remodeling (PLR) (8–10). Recent advancements in optical imaging have provided morphologic evidence for the degeneration of the LCN and the osteocyte network with age (11–13), but how these architectural changes to the osteocyte network impact aged-bone health remains unclear.

Aged bone demonstrates several defects including losses in mechanostimulation (14), uncoupling of bone deposition and resorption (1, 2), alterations to bone material properties (15, 16), and degeneration of the LCN (17). Mechanical loading applied at the organ scale compresses the mineralized bone tissue driving interstitial fluid flow through the organic pericellular matrix that lines the mineralized walls of the LCN (18–21), with the resulting fluid-induced stresses and strains in osteocytes transduced into biochemical cues. Osteocytes respond to fluid flow with increased expression of bone anabolic genes and a corresponding increase in bone formation in young, murine tibial loading studies (22). However, bones from middle-aged mice experience tempered responses to loads that progressively worsen with age (1, 14, 23, 24). Additionally, osteocytic PLR maintains bone-matrix material properties, one of several aspects of bone quality that decline with age, leading to the increased risk of fragility fractures in elderly individuals, even those with clinically normal bone mass (8, 9, 25–28). Age also takes a toll on the osteocyte LCN, with a loss of canaliculi and changes in lacunar geometries in old bone (11, 13, 29). Similarly, microcracks caused by fatigue loading can cause severe localized damage to the LCN, with a loss of connectivity and nutrient supply leaving local osteocytes vulnerable and preventing local adaptive remodeling (30). Because osteocytes rely on the LCN for mechanosensation and for coordinating bone remodeling to maintain bone mass and quality, we hypothesized that the age-related degeneration of the

Significance

Bone fragility increases with age as the result of the concurrent decline of bone mass, quality, and mechanosensitivity. While the coordinated decline of these behaviors remains unexplained, the role of osteocytes in each of these processes and the age-related degeneration of the lacunocanalicular network (LCN) in which they reside implicate osteocytes in bone aging. In this work, we identify canalicular loss as a driver behind declining mass transport and mechanostimulation within the LCN of aged bone and of bone with osteocyte-intrinsic defects in transforming growth factor beta signaling. We identify the ability to restore physical stimulation to osteocytes through expansion of the pericellular space. Future studies will determine if therapeutic stimulation of osteocyte function can improve bone health with age.

Author contributions: C.A.S., S.W.V., and T.A. designed research; C.A.S. and S.W.V. performed research; C.A.S. and S.W.V. contributed new reagents/analytic tools; C.A.S. and S.W.V. analyzed data; and C.A.S. and T.A. wrote the paper.

The authors declare no competing interest.

This article is a PNAS Direct Submission. M.B.S. is a guest editor invited by the Editorial Board.

[1]To whom correspondence may be addressed. Email: tamara.alliston@ucsf.edu.

This article contains supporting information online at https://www.pnas.org/lookup/suppl/doi:10.1073/pnas.2023999118/-/DCSupplemental.

Published June 14, 2021.

LCN plays a causal role in the decline in bone health and increased skeletal fragility in aging.

Several hallmarks of aged bone also appear in bone from mice with limited transforming growth factor beta (TGF-β) signaling, including impaired mechanical adaptation, poor bone quality, and LCN degeneration. First, in mice that express a dominant negative version of TGF-β receptor type II (TβRII), bone apposition in response to loading was significantly impaired compared with wild-type controls, implicating intact TGF-β signaling in the anabolic response of bone to mechanical stimulation (31). Second, osteocyte-intrinsic ablation of TβRII (TβRII$^{ocy-/-}$) causes severe bone-quality defects without meaningful changes to cortical bone mass, including reduced fracture toughness (9). Third, silver nitrate staining of the LCN shows that bones from TβRII$^{ocy-/-}$ mice have a shortened canalicular phenotype, which is attributed to the coordinated repression of genes required for PLR such as MMP13, MMP14, and Cathepsin K (9, 32). Thus, a similar set of bone phenotypes arise from the systemic effects of aging and from the osteocyte-intrinsic effects of TβRII ablation. However, the extent to which these similarities are mechanistically related remains unclear. Either way, given the importance of TGF-β in fracture repair, osteogenesis imperfecta (33), Camurati–Engelman disease (34), and other human skeletal syndromes (35), understanding the role of TGF-β in maintaining the LCN and bone strength may give insight to clinical bone fragility.

Functional analysis of the osteocyte LCN faces challenges in isolating and manipulating specific LCN features, especially within the complex, mineralized extracellular matrix (ECM). Here, we apply quantitative in silico approaches to probe the function of osteocyte networks visualized deep within cortical bone using confocal laser scanning microscopy (11–13). We test the hypothesis that LCN degeneration, whether due to systemic aging or osteocyte-intrinsic TGF-β deficiency, compromises osteocyte mass transport and mechanosensation. Unraveling the functional consequences of LCN degeneration could advance the search for therapeutically tractable mechanisms to improve bone mass or bone quality with age.

Results

Suppressed TβRII Levels and Canalicular Architecture in Aged and TβRII$^{ocy-/-}$ Bone. The reported degeneration of the LCN with aging (11, 17) led us to examine the effect of aging on skeletal gene expression in osteocyte-enriched cortical bone. We used NanoString arrays, including a custom array of over 800 genes associated with skeletal cell differentiation, ECM remodeling, and relevant signaling pathways such as Wnt, PTH, and TGF-β. Relative to young mouse cortical bone (2 mo), genes implicated in ECM remodeling and TGF-β signaling were among the most strongly repressed in aging (36 mo) (Fig. 1*A*). The age-dependent LCN degeneration corresponded with the repression of MMP13, MMP14, and other ECM remodeling enzymes implicated in osteocyte PLR, a process that supports the maintenance of the LCN (8–10, 32). Investigation of all genes within the Kyoto Encyclopedia of Genes and Genomes (KEGG) TGF-β signaling pathway included in the NanoString arrrays showed systematic deregulation of TGF-β signaling with aging (Fig. 1 *A* and *B*, black bars). The most significantly repressed genes are those encoding the canonical TGF-β R-Smad (Smad3) and TGF-β target genes Smad6 and Ski. Systemic aging also leads to the repression of TβRII in bone, with a magnitude comparable to that observed in mice with genetic ablation of a floxed Tgfbr2 allele in osteocytes under control of 10 kb DMP1-Cre, relative to Cre-negative controls (Fig. 1*B*, gray bars). Also, like aging bone, bone from TβRII$^{ocy-/-}$ mice also express low levels of MMP13 and MMP14 (9).

Whether due to aging or to osteocytic Tgfbr2 deficiency, the deterioration of the osteoctye LCN is evident. Staining of the LCN in paraffin sections shows the sparse canaliculi in old or TβRII$^{ocy-/-}$ bone relative to young or TβRII^{ctrl} bone (Fig. 1 *C*–*F*). Quantitative analysis shows that, relative to their controls, the average canalicular length is reduced in both old and TβRII$^{ocy-/-}$ bone, and they are statistically indistinguishable between each other (Fig. 1*G*). Therefore, to understand the functional impact of LCN degeneration resulting either from systemic aging or from osteocyte-intrinsic defects in TGF-β signaling, we evaluated LCN structure and function in each of these two mouse models.

Limitations of visualizing this elaborate three-dimensional (3D) network in thin paraffin sections led us to examine the LCN using fluorescent confocal microscopy of thick cleared cortical bone sections (Fig. 1 *H*–*O*). These detailed 3D images strikingly reveal the loss of canalicular density and organization in aged or TβRII$^{ocy-/-}$ bone (Movie S1). Quantitative analysis of these images shows that the shortened canalicular phenotype of aged or TβRII$^{ocy-/-}$ bone, apparent in paraffin sections (Fig. 1*G*), in part results from canaliculi bending in and out of the focal plane due to increased canalicular tortuosity, τ, (Fig. 1*P*).

Consistent with previous findings, canalicular architecture is altered by defective TGF-β signaling without changes to lacunar number as previously noted by synchrotron radiation microtomography (SRμT) (9), but both lacunar and canalicular features deteriorate with age (11, 13) (Fig. 1 *Q* and *R*). Analyses of canalicular features revealed similar patterns of canalicular alterations in aged and TβRII$^{ocy-/-}$ bone relative to controls, with reduced canalicular dendrite numbers (Fig. 1*R*) observed through Imaris-aided quantification of the direct canalicular sprouting point before the first bifurcation (S.1), as well as a reduced LCN volume fraction and increased canalicular spacing (Fig. 1 *S* and *T*). How these changes to osteocyte canalicular architecture precisely impact cellular performance is unknown.

Maintenance of Network Architecture but Loss of Nodal Interactions with Age and TGF-β Signaling Disruption. Given the challenges in manipulating and observing osteocyte networks in vivo and in vitro, we applied in silico approaches to probe the functional implications of LCN degeneration on osteocyte connectivity, mass transport, and mechanosensitivity. First, using network scale connectomic analysis, a nondimensional collection of nodes and edges is constructed on top of 3D osteocyte networks derived from bone of young and old, or TβRII^{ctrl} and TβRII$^{ocy-/-}$, mice (Fig. 2*A*) (36, 37). Nodal analysis provides important insight into the prevalence and type of canalicular junctions, which can impact solute transport and fluid mechanics (38).

Although the average number of nodes was decreased in both the aged and TβRII$^{ocy-/-}$ models compared with young or Cre-negative controls (Fig. 2*B*), underlying aspects of network architecture are unaffected by LCN degeneration. For example, mean node degree (n), a measure of network architecture that reflects the number of connected nearest neighbors, is equal across all groups when excluding end-point nodes (Fig. 2 *C*, *Left*), emphasizing high-level maintenance of network organization. Furthermore, while the osteocyte density within the connectomes was kept constant to prioritize canalicular path behavior (Fig. 2*D*), the primary node types (t and c nodes) remain proportionally constant with age or with TGF-β deficiency (Fig. 2 *E* and *F*). However, increases in the number of end-point nodes in the LCN of aged and TβRII$^{ocy-/-}$ bone stratified them from their controls (Fig. 2*G*). The increase in end-point nodes ($n = 1$) in aged and TβRII$^{ocy-/-}$ networks significantly affects LCN architecture by lowering the mean node degree (Fig. 2 *C*, *Right*) by identifying an increase in nonfunctional path choices in which canaliculi terminate within the matrix without reconnecting to the network, revealing higher numbers of discontinuities at the termini of canaliculi in degenerated models. Investigation of branching through segmentation of canalicular features at regular concentric distances away from the cell body (Fig. 2*H*) shows that, although degenerated models lose canalicular number at the root (Fig. 2*I*), remaining canaliculi in the aged and TβRII$^{ocy-/-}$ models expand at similar rates to controls

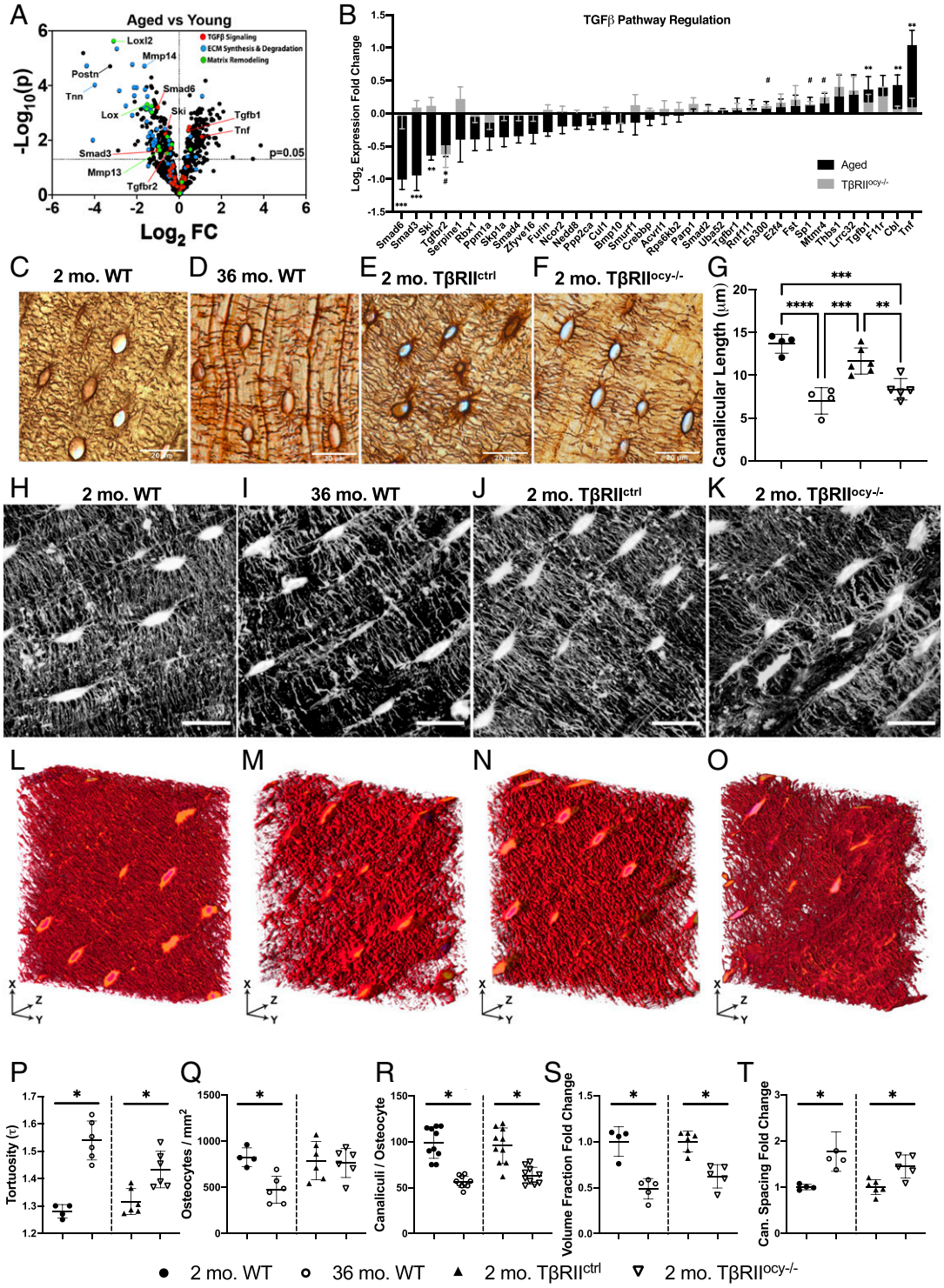

Fig. 1. Aged and TβRII$^{ocy-/-}$ bone share molecular and canalicular morphologic changes. (*A*) Volcano plot of 800+ genes from NanoString panels shows down-regulation of genes involved in matrix interaction and remodeling in aged bones. (*B*) Log_2 expression fold change of TGF-β signaling pathway genes from NanoString showing systematic regulation with age (36 mo, $n = 4$ versus 2 mo, $n = 3$, black bars). RNA from TβRII$^{ocy-/-}$ bone shows significant repression of only Tgfbr2 (TβRII$^{ocy-/-}$ versus TβRII^{ctrl}, $n = 4$ each, gray bars). *Significant effect w.r.t. age; #significant effect w.r.t. TβRII$^{ocy-/-}$; $*P < 0.05$, $**P < 0.01$, and $***P < 0.001$ by Student's *t* test. Silver nitrate staining (*C*–*F*) of the osteocyte LCNs showing shortened canalicular lengths in 2D at 36 mo ($n = 4$) or with disrupted TGF-β signaling ($n = 5$) (Scale bar, 20 μm). Young C57BL/6 mice ($n = 4$) showed no significant differences in canalicular length to TβRII^{ctrl} mice ($n = 6$); additionally, mice with ablated TGF-β signaling showed no significant differences from aged mice in multiple post hoc Tukey-corrected pair-wise comparisons. (*G*) $**P < 0.01$, $***P < 0.001$, $****P < 0.0001$. Maximum *z*-projections (*H*–*K*) of a single plane of osteocytes (~12 μm). (Scale bar, 20 μm.) (*L*–*O*) 3D reconstructions of 75- × 75- × ~35-μm sections of LCN captured by confocal imaging showing loss of canaliculi and canalicular organization in aged (*I* and *M*) ($n = 6$) and TβRII$^{ocy-/-}$ (*K* and *O*) ($n = 6$) mice compared with 2-mo WT controls (*H* and *L*) ($n = 4$) and 2-mo TβRII^{ctrl} mice (*J* and *N*) ($n = 6$), respectively. Quantification of LCN parameters completed in 3D within a 30-μm–thick selection (*P*–*T*) shows similar changes in aged and TβRII$^{ocy-/-}$ bone, with the exception of osteocyte area density (*Q*) showing loss of cell bodies in only aged bone. $*P < 0.05$ by Student's *t* test to proper control.

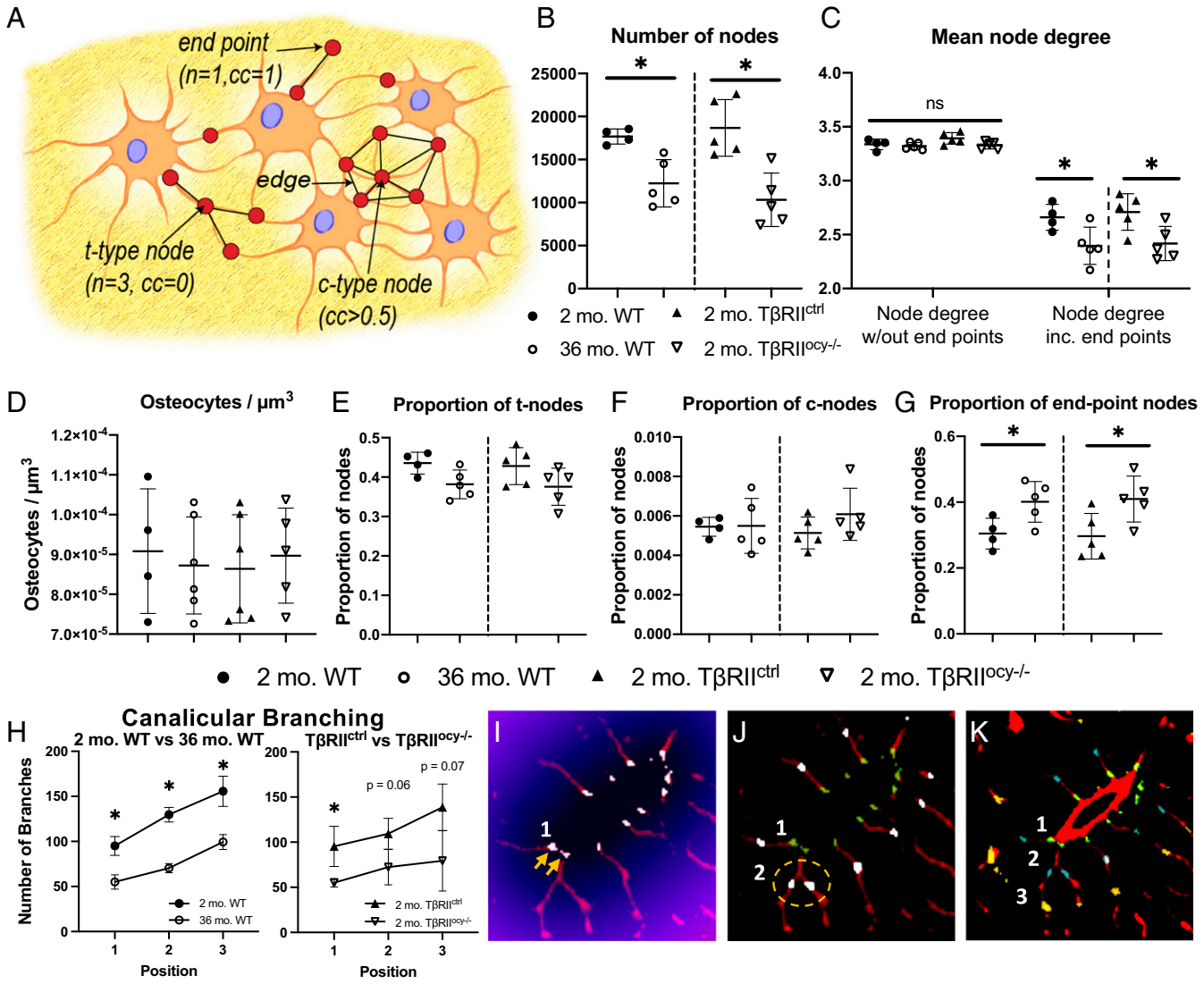

Fig. 2. Nodal analysis shows maintenance of network architecture but loss of total network interactions with age and TGF-β signaling disruption in osteocytes. Individual node classification (*A*) from connectomic analysis of the LCN from skeletonized confocal images shows a dramatic loss of total identified nodes (*B*) in aged and TβRII$^{ocy-/-}$ bone compared with controls. Mean node degree (connections per node) without considering end-point nodes (*C*, *Left*) shows maintenance of the underlying network architecture even with degeneration. In contrast, inclusion of end-point nodes (*C*, *Right*) demonstrates the detrimental effect of disjointed paths in the network. While maintaining equal osteocyte number within volumes studied (*D*), the relative proportion of branch-like t nodes (*E*) and cluster-like c nodes (*F*) persisted across all models, while there was an increase in the proportion of end-point nodes (*G*) in degenerated models. Canalicular branching identified through segmentation in expanding concentric positions away from the cell body (*H*) reveals degenerated models showed specific loss of canalicular number at the sprouting point (*I*, yellow arrows) but continued to branch normally at the first region of bifurcation (*J*, dashed yellow) and again further into the network (*K*, yellow). *$P < 0.05$ to young, WT controls. $n = 5$ for all groups.

within the first region of canalicular bifurcation (Fig. 2*J*, white) and again further into the network (Fig. 2*K*, yellow). Therefore, as the LCN ages in cortical bone, rather than changing canalicular organization and adopting a more web-like state, as found in woven bone (36, 37, 39), it undergoes pruning by which dendrites retract or degenerate, but branching near cell bodies is unaffected.

Aged and TβRII$^{ocy-/-}$ Osteocyte Networks Have Impaired Transport Capabilities. While higher-order LCN structure is preserved with age and TGF-β disruption, the loss of canaliculi and canalicular junctions may limit fluid and solute movement. If mass transport through the LCN is compromised, it could influence osteocyte nutrient exchange and the ability of osteocytes to signal with one another and with other cell types. Therefore, to determine the effect of LCN degeneration on mass transport, we applied betweenness centrality (BC) analysis to the LCN connectomes of young and old and TβRII^{ctrl} and TβRII$^{ocy-/-}$ bones. BC is defined as the fraction of shortest paths within a network running through any particular node (Fig. 3*E*), in which high-BC scoring nodes represent heavily used paths (Fig. 3 *A*–*D*). Nodes that appear in at least 1% of paths within the connectome are shown in color, with red nodes being the most heavily utilized.

Using BC analysis, we find that with age or osteocytic TGF-β deficiency, the number of available paths is reduced, with the obvious consequence that remaining paths are much more heavily utilized. Specifically, the proportion of nodes scoring above the 1% threshold is increased in the LCN of aged and TβRII$^{ocy-/-}$ bones compared with their young and TβRII^{ctrl} controls (Fig. 3*F*). Low-scoring nodes (blue, BC = 0.01 to 0.1) abundant in healthy, young bone dissipate in the degenerated models, indicating fewer

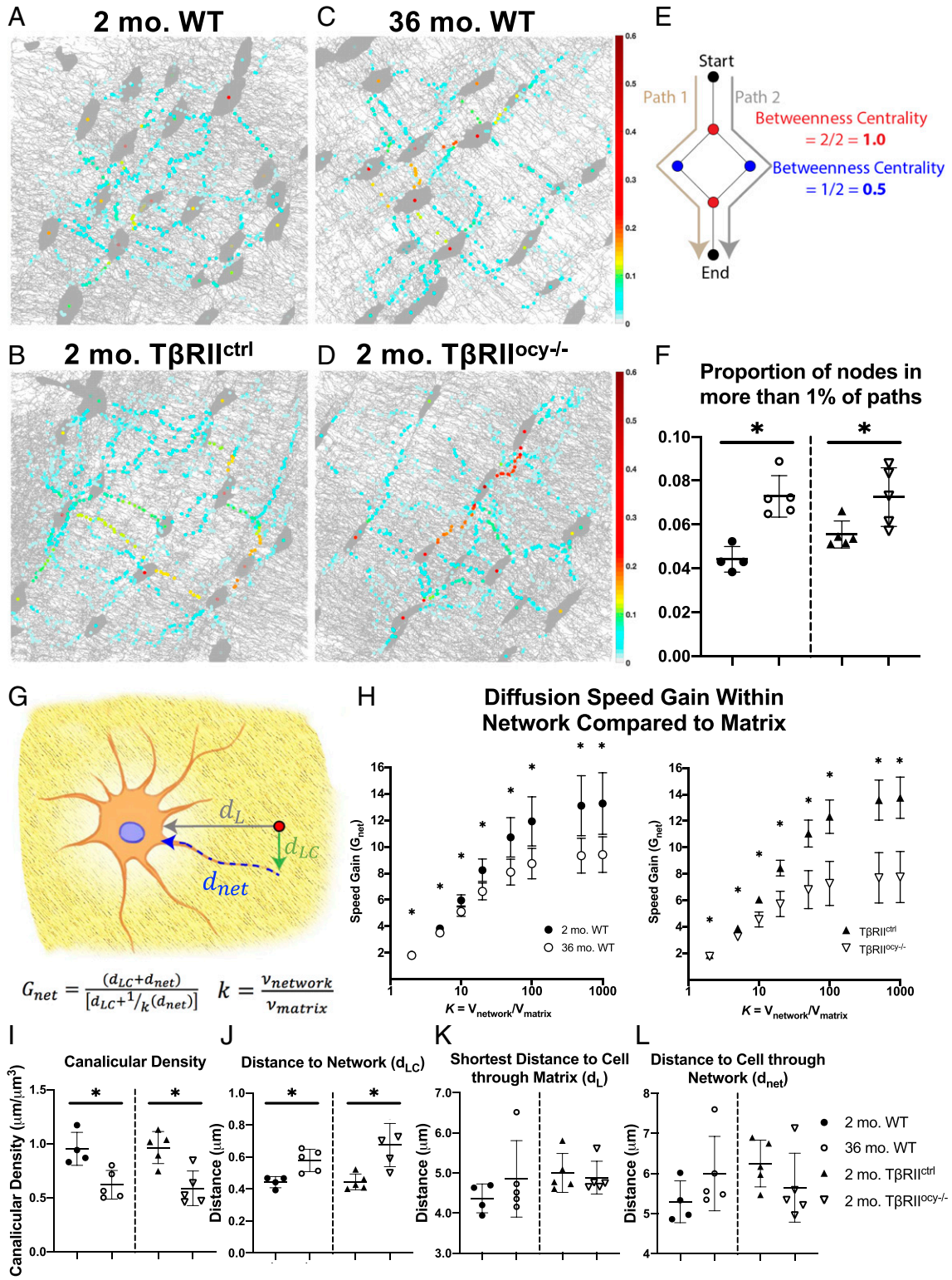

Fig. 3. Aged and TβRII$^{ocy-/-}$ osteocyte networks have limited pathway availability and lower transport capabilities in in silico connectomic models. Projection of 3D skeletonized maps of the LCN with nodes color-mapped to their individual BC values (*A–D*). Color bar indicates BC score for individually plotted nodes. (*E*) Schematic example for the calculation of Betweenness Centrality for individual nodes within a given network. Higher BC-scoring nodes align to show heavily used pathways within the network (BC > 0.01), with a higher fraction in degenerated models (*F*) indicating more limited pathway choice. See Movies S2 and S3 for 3D representation. Comparison of transport capacity within bone from the skeletonized connectomic-network models shows an increase in nondimensional diffusive speed gain (*G*) in networks of young, control bones compared with respective degenerated models (*H*). This is primarily driven by a decrease to canalicular length density (*I*) in degenerated models increasing distance to the LCN from the matrix (d_{LC}, *J*) rather than an increase in distance to the nearest cell directly through the matrix (d_L, *K*) or from points within the LCN to the nearest lacuna through the network (d_{net}, *L*). *$P < 0.05$. $n = 5$ for all groups.

available paths for mass transport within the networks. In contrast, fewer paths exists in old or TβRII$^{ocy-/-}$ bone and are much more heavily utilized (yellow-red, BC > 0.1), features that are readily apparent in videos showing BC values within the 3D connectomes (Movies S2 and S3). Therefore, greater reliance on fewer pathways with age is a feature of these compromised networks.

We next modeled the effect of LCN degeneration on its ability to complete a diffusive task using measured network distances and physical diffusion constants (Fig. 3*G*). With a smaller diffusive speed gain than controls, the aged LCN has a diminished ability to shuttle material through the network (Fig. 3*H*). The effect of aging on the diffusivity of the LCN was almost identical to that resulting from osteocyte-intrinsic loss of TGF-β signaling (Fig. 3*H*). In both cases, the diminished diffusivity is largely due to the decreased canalicular density (Fig. 3*I*). With ∼40% lower canalicular length density, the distance a molecule must travel to get from the ECM to the LCN (d_{LC}, Fig. 3*J*) is significantly increased in degenerated networks compared with their respective controls. Other variables that affect diffusive speed gain (d_L and d_{net}, Fig. 3 *K* and *L*) remain unchanged by LCN degeneration in these models. Intuitively, this analysis shows that, of the many LCN features disrupted by aging or osteocytic TGF-β deficiency, including canalicular number and tortuosity, the loss of canalicular number or density is the most important driver of the reduced diffusivity in this model.

Fluid-Dynamics Modeling Demonstrates Lower Fluid Velocity and Shear Stress as a Function of Pericellular Space Volume and Not Canalicular Tortuosity. Given the importance of the LCN for osteocyte mechanosensation, we sought to determine how LCN fluid-flow shear stress changes following LCN degeneration due to either systemic aging or osteocyte-intrinsic suppression of TGF-β signaling. To that end, we used computational fluid dynamics to model load-induced interstitial fluid flow within the pericellular space (PCS) surrounding single osteocytes (Fig. 4*A*). Standard PCS volumes were modeled from the same set of confocal fluorescence images of osteocyte networks from young and old and TβRII^{ctrl} and TβRII$^{ocy-/-}$ bone (Fig. 4*B*). Computational complexity limited our analysis to individual osteocytes, which were segmented consistently to eliminate confounding local features such as blood vessels. Using these models, we can easily modify the dimensions of the PCS parametrically to mimic volume changes caused by the suppression (0.5×, Fig. 4*C*) or induction (2×, Fig. 4*D*) of PLR remodeling. Even at the single-cell scale, the loss of osteocyte surface area in aged and TβRII$^{ocy-/-}$ bone is still evident (Fig. 4*E*). The twofold in silico changes in PCS thickness roughly double or half the total calculated volume of the modeled LCNs within each group, whereas differences between young and old or TβRII^{ctrl} and TβRII$^{ocy-/-}$ bone account for no more than a 60% change in PCS volume (Fig. 4*F*).

Modeling of interstitial fluid flow at constant volume and pressure revealed profound differences in the shear-stress magnitude and distribution in the PCS of old and TβRII$^{ocy-/-}$ osteocytes relative to their young or TβRII^{ctrl} controls (Fig. 5*A*). Maximum fluid velocities of 686.95 μm/s around young osteocytes, and, similarly, 525.70 μm/s for TβRII^{ctrl} osteocytes, were approximately double those predicted for osteocytes from aged and TβRII$^{ocy-/-}$ bones, at 242.82 μm/s and 321.86 μm/s, respectively (Fig. 5*B*). Likewise, maximum shear stresses are significantly higher for young and TβRII^{ctrl} osteocytes than for aged and TβRII$^{ocy-/-}$ cells (Fig. 5*C*).

These reductions in fluid velocity and shear stress with LCN degeneration could arise from several factors such as changes in canalicular length (Fig. 1*G*), LCN or PCS volume (Figs. 1*T* and 4*G*), or tortuosity (Fig. 1*Q*). Using fluid dynamics modeling, we tested the contribution of PCS volume and tortuosity to fluid-flow shear stress. We were surprised to find, by modeling fluid flow in individual canaliculi across a range of tortuosity, that increasing tortuosity had no significant effect on either fluid velocity or shear stress (Fig. 5*D*). This suggests that osteocytes in degenerated networks do not gain any mechanosensitive advantage by generating canalicular tortuosity.

On the other hand, the expanded PCS volume and the resulting increased flow rates generated significantly greater maximum fluid velocities than in baseline conditions, while constriction of this space had the opposite effect (Fig. 5*E*). Remarkably, PCS expansion increased the fluid flow velocity and shear stress predicted for aged or TβRII$^{ocy-/-}$ osteocytes such that these values were statistically indistinguishable from young or TβRII^{ctrl} controls at baseline PCS volumes (Fig. 5 *F* and *G*). These findings emphasize the importance of PCS volume on osteocyte pericellular fluid movement and highlight the potential to rescue impaired osteocyte mechanosensation due to LCN degeneration in aging by increasing PCS volume.

Discussion

This study provides evidence that the decline of bone health with age is mechanobiologically linked to the age-related degeneration of osteocyte LCN structure and function. By examining the functional implications of LCN degeneration on osteocyte mass transport and pericellular fluid flow, this work informs the biological and physical decline of bone during aging and suggests strategies to defend against this loss. Specifically, by utilizing a combination of in silico analyses, we identified that reductions in canalicular number and connections reduce diffusion within the LCN and pericellular fluid velocity, a driver of osteocyte mechanosensation. Connectomics analysis revealed the LCN architectural changes that occur with age in cortical bone and how LCN pruning limited pathway availability and mass transport in old bone. Finite element (FE) modeling identified that loss of osteocyte canaliculi alone is sufficient to reduce the LCN surface area and limit shear mechanostimulation along this surface. Finally, FE modeling showed that deficits to fluid velocity and associated shear of aged osteocytes are recoverable by increasing PCS volume even without changing the remaining architecture of the LCN. These observations apply whether LCN degeneration results from systemic aging or from a targeted defect in osteocytic TGF-β signaling. Thus, this work identifies lost fluid dynamics and mechanostimulation as consequences of LCN pruning in response to osteocyte TGF-β deficiency or aging and provides evidence that restoration of osteocyte stimulation through pericellular fluid flow is physically possible without the need to regrow lost canaliculi.

A key strength of this study is the ability to distinguish the functional effects of lacunar and canalicular changes by comparing LCN degeneration in aging and TβRII$^{ocy-/-}$ mice. Previous studies of the LCN of aged bone note canalicular losses as well as diminished osteocyte number and lacunar size (11, 13, 29), confounding the ability to dissect lacunar and canalicular contributions to LCN function. On the other hand, TβRII$^{ocy-/-}$ bone lost canaliculi to the same extent as aged bone with no change in lacunar number. This finding using optical imaging is similar to previous findings in this model using SRμT, documenting no loss to lacunar number with TGF-β signaling disruption (9), highlighting the ability to assess the contribution of the canalicular network to osteocyte function and health using this model. Therefore, canalicular loss, in either model, is sufficient to compromise key aspects of osteocyte function including mass transport and mechanosensation.

As in TβRII$^{ocy-/-}$ bone (9), aged bone showed suppression of genes encoding TβRII and PLR enzymes. Since PLR supports the maintenance of the osteocyte LCN (10, 40), reduced TGF-β signaling may play a causal role in the age-related degeneration of the LCN. While the molecular mechanism responsible for declining TGF-β signaling and PLR with age in bone has yet to be explored, this work establishes that both aged and TβRII$^{ocy-/-}$ bone share canalicular defects that impair the LCN in both form and function. Although the effects of DMP1-Cre/TβRII$^{fl/fl}$ on

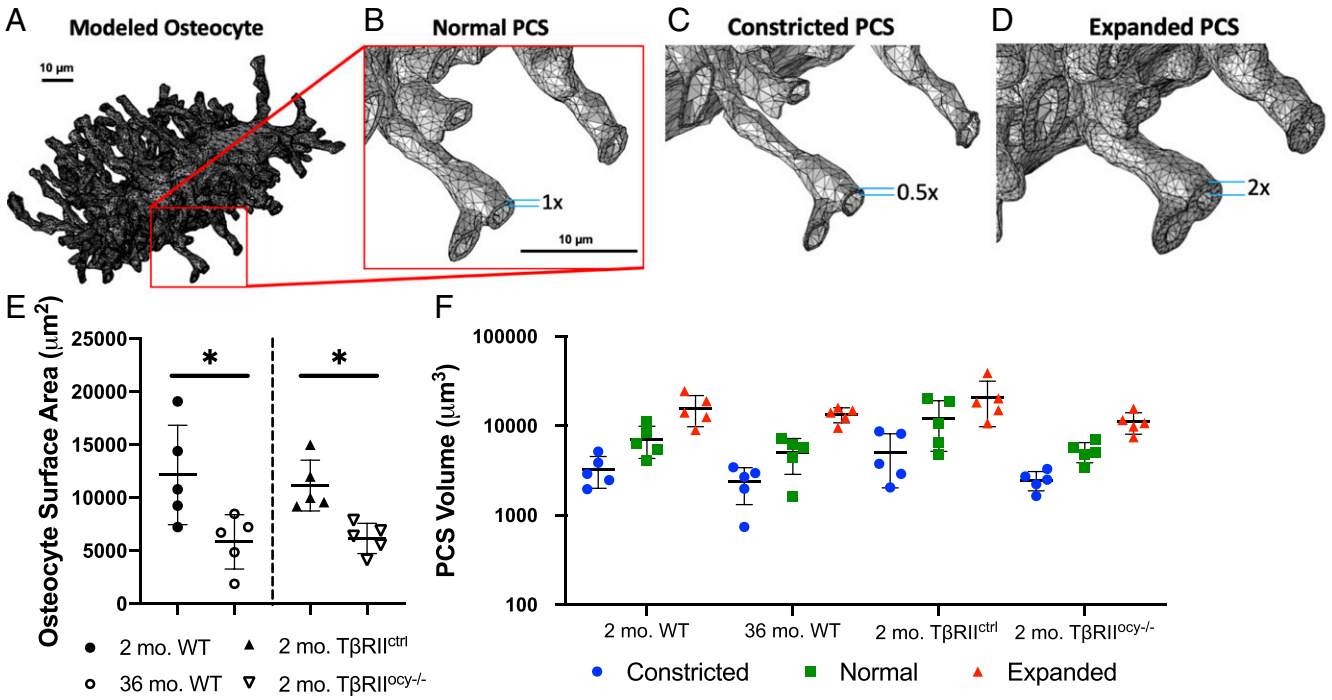

Fig. 4. FE models of individual osteocytes. (*A*) Meshing of individual osteocytes and (*B*) modeling of surrounding PCS at standard width (0.08 μm) and constricted or expanded width by a factor of 2 (*C* and *D*, 0.04 and 0.16 μm, respectively). Osteocyte surface area (*E*) varied between controls and degenerated models. Manipulation of PCS thickness caused commensurate changes in PCS volume (*F*), with greater changes within groups (age/genotype) at different PCS thicknesses than between groups at the same PCS thickness.

osteocyte morphology and health have previously been recapitulated through pharmaceutical inhibition of TGF-β signaling in skeletally mature mice (9), it is important to note that the constitutive nature of the removal of TβRII through DMP1 may also occur in "late-stage" osteoblasts as they begin their transition into osteocytes. While this may result in some lingering developmental defects impacting the osteoblast–osteocyte transition, and is thus unrelated biologically to the aged-related loss of canaliculi, the TβRII$^{ocy-/-}$ phenotype is still canalicular specific and also subtle compared with other models of altered TGF-β signaling within the skeleton, where phenotypes are much more severe (33, 34). Additionally, disruptions to TFG-β signaling are independently observed in our NanoString analysis of aged osteocytes including, specifically, TβRII, supporting the rationale to utilize this mouse model in parallel with aged mice. To definitively address the role of TGF-β signaling in mature osteocytes within the LCN, the use of an inducible Cre mouse without additional skeletal effects is desired, while our model is sufficient in understanding the canalicular contributions to LCN degeneration.

These imaging and computational analyses point to the role of canalicular loss and pruning in LCN degeneration in both aged and TβRII$^{ocy-/-}$ bone. LCN pruning can occur prior to or independently of osteocyte death, since canalicular density is low in TβRII$^{ocy-/-}$ bone even when osteocyte density is preserved. Concentric canalicular feature identification showed a primary defect of whole canalicular loss in degenerated models while remaining dendrites branch and expand normally, while end-point nodal classification identifies pruning at the distal end of processes as they withdraw from the network, severing connectivity. Both these alterations to the network compromise the size and pervasiveness of the network throughout the bone matrix and, along with previous work estimating the size limit for particle diffusion through the LCN of 40 kD (41, 42), compromise osteocyte function. This is supported by our findings that predict a 30 to 45% reduction in the speed of particle movement through degenerated networks. These limitations to mass transport within bone impact all three major bone-cell types, since osteocytes rely on the LCN for nutrient supply (25) as well as for signaling to osteoclasts and osteoblasts. Thus, canalicular morphology is altered in multiple ways, raising further questions about the different biologic processes that control different aspects of canalicular morphology and how this may impact cellular cross talk, bone remodeling, and the decline in bone mass and bone quality with age (43).

Fluid flow within the LCN is a primary mechanism by which mechanical stimulation drives bone anabolism, a response that is diminished in aged bone (44) that additionally depends on canalicular path availability. While fluid shear stress has previously been postulated to stimulate osteocytes, presented here as a functional outcome/defect, it is likely that the fluid stimulation occurs via fluid drag–induced strain at molecular attachments and focal adhesions along canalicular dendrites and the canalicular wall (42, 45). Therefore, the changes in velocities reported here likely have commensurate effects on the strain stimulation of the osteocytes as has been shown in previous modeling studies (19, 46–48). While losses of osteocyte cell bodies and changes to lacunar geometry toward smaller and rounder lacunae with age (13, 49) have already been implicated in reduced fluid flow in the LCN (50), here, we report complementary canalicular changes with age. Given that the osteocyte canaliculi are predicted to be the primary mechanosensing portion of the LCN (51, 52), knowledge of which of these geometric changes most diminishes fluid flow remains a significant knowledge gap.

Our prior work using idealized canalicular models predicted that tortuosity would slightly increase localized mechanical stimulation (19). Thus, we hypothesized that the increased canalicular tortuosity may allow aged or TβRII$^{ocy-/-}$ osteocytes to increase local mechanical stimulation. Streamline plots qualitatively identified local regions of enhanced fluid shear around canalicular bends, but these hotspots were insufficient to overcome the greater loss of fluid velocity and shear stimulation caused by canalicular loss. Because

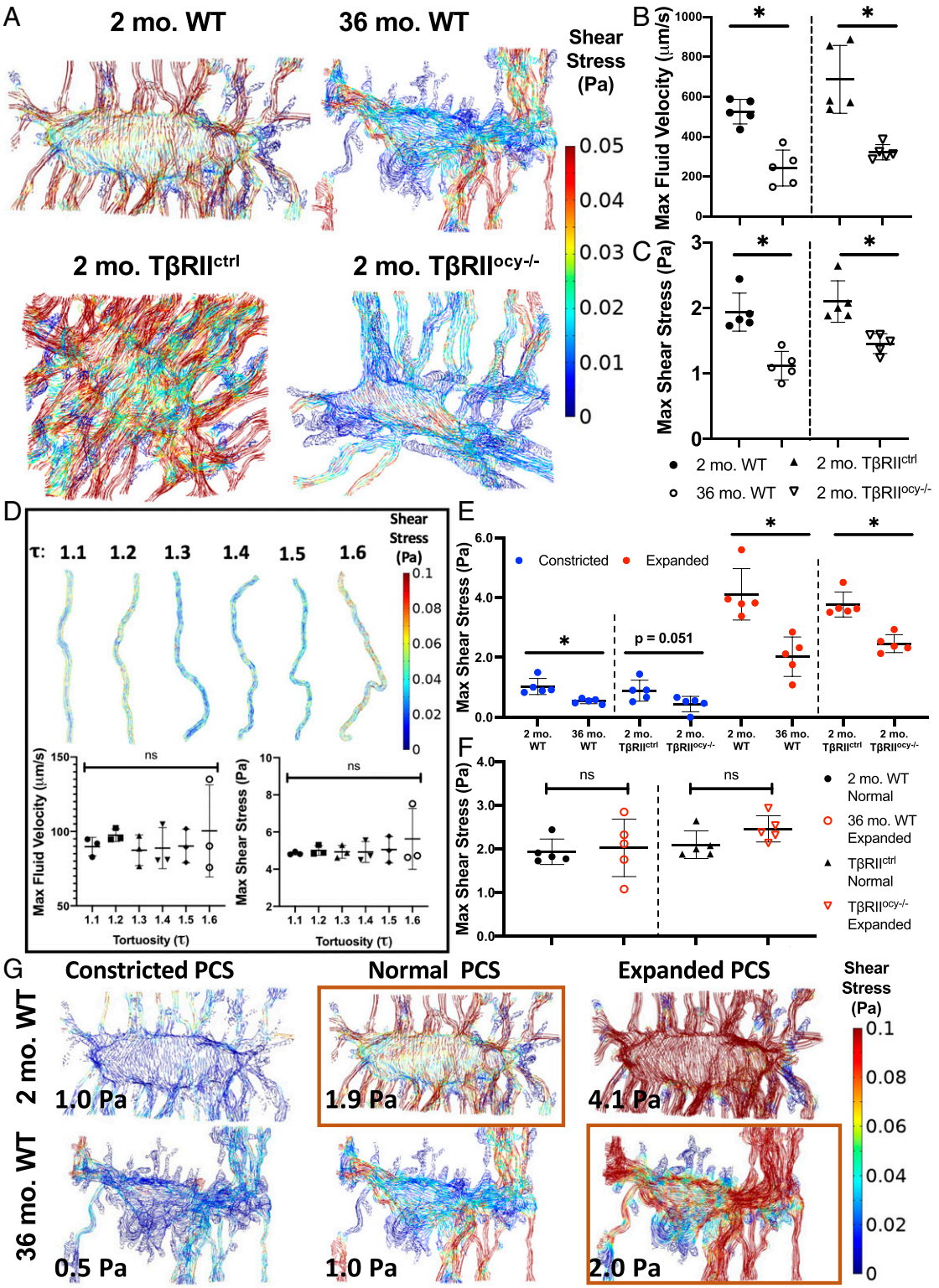

Fig. 5. Fluid-dynamics modeling demonstrates lower fluid velocity and shear stress as a function of PCS volume and not canalicular morphology. Visualization of streamlines (*A*) and quantification of fluid flow within the PCS around single osteocytes from both aged and TβRII$^{ocy-/-}$ show significant reductions to fluid velocity and shear stress compared with controls (*B* and *C* $n = 5$ and 3 individual cells per *n*). In contrast, no appreciable change in flow within single canaliculi (*D*) of varying tortuosities was observed. Parametric modulation of PCS volume around the same osteocyte geometries maintains trends between models as seen in the base condition, but overall magnitude changes when the PCS is constricted or expanded (*E*). Expansion of the PCS in degenerated models recovers shear-stress values to levels comparable to young controls at standard PCS volume (*F*). Streamline visualization of the effect of volume modulation (*G*) shows recovery of shear magnitude for aged osteocytes with an expanded PCS volume to that observed for young osteocytes (outlined in orange). *$P < 0.05$.

these models applied a uniform baseline PCS thickness of 0.08 μm derived from prior studies, the effects of other known local changes in canaliculi are undetectable in this model, such as canalicular hillocks near tethering elements (42, 53, 54). Nonetheless, these models demonstrate the importance of LCN surface area and canalicular loss on fluid stimulation.

Despite localized increases in canalicular shear, we were surprised to find that the severe bending of canaliculi in aged and TβRII$^{ocy-/-}$ bone is insufficient to overcome the losses in physical stimulation in the models caused by the broader degeneration of the LCN. Inclusion of proteoglycan tethering elements may reduce the magnitude of lost stimulation in these models. However, since mechanostimulation at either the surface of the canalicular dendrite or on perpendicular tethering elements will increase or decrease with flow velocity, this finding refutes the idea that control of canalicular geometry alone is a meaningful way to restore lost mechanical stimulation with age driven by the broader loss of LCN volume that is the result of pruning.

On the other hand, osteocytes have the capacity to modulate the size and quality of their PCS through PLR (10, 55). For example, relative to bone from virgin control mice, canalicular diameter increases by 20 to 30% with lactation and returns to baseline after weaning (55), demonstrating expansion and constriction of the local PCS. Our fluid-dynamics modeling demonstrates the important functional implications of changing PCS diameter through a process like PLR. First, a 50% constriction of the young wild-type osteocyte PCS renders a shear stress that matches aged and TβRII$^{ocy-/-}$ osteocytes at baseline PCS thickness. Second, doubling the PCS of aged and TβRII$^{ocy-/-}$ osteocytes returned shear stress to levels that were indistinguishable from young or wild-type controls. How these changes to the PCS impact the proteoglycan-rich pericellular matrix and its modulation of local fluid drag or tensional homeostasis (56) remains to be determined. Nonetheless, control of the PCS, possibly through PLR, presents a mechanism by which osteocytes can homeostatically adapt their mechanical microenvironment to reclaim meaningful amounts of lost physical stimulation in age and disease, although further resorption of bone would need to be carefully considered in osteoporotic cases.

This in silico work highlights the opportunity to overcome experimental complexities inherent in studying the relationship between osteocyte LCN structure and function. Of the many LCN features sensitive to age (11, 13) or TGF-β deficiency (9), these computational models allowed us to identify those that are most important for the impaired mechanosensitivity of bone in each model (14, 38, 48). Given the important role of PCS volume, agents that regulate PLR emerge as potential therapeutic candidates to restore function lost in aged bone and motivate further study.

Materials and Methods

See *SI Appendix* for extended methods.

Mice. Inbred, male C57BL/6 mice (wild type, WT) (young, 2 mo, $n = 4$ and aged, 36 mo, $n = 5$) from the Buck Institute for Research on Aging were used for comparisons regarding age-related phenotypes. A line of male mice with established ablation of TβRII in osteocytes under control of −10 kb DMP1-Cre (TβRII$^{ocy-/-}$) (9) (2 mo, $n = 5$) and their Cre-negative litter mate controls (TβRII^{ctrl}) (2 mo, $n = 5$) on a mixed-C57BL/6 background were used as a model of LCN degeneration for comparisons with aged phenotypes. All animal procedures were approved by the Institutional Animal Care and Use Committee of the University of California San Francisco (UCSF) and the Buck Institute for Research on Aging.

RNA Expression Analysis. Messenger RNA from osteocyte-enriched cortical bone was collected as previously described (49, 57) from young (2 mo, $n = 3$) and aged (36 mo, $n = 4$) C57BL/6, WT mice and TβRII$^{ocy-/-}$ and TβRII^{ctrl} littermates ($n = 4$ per genotype). The raw mRNA sequence expression from a preselected subset of 813 genes was quantified from purified RNA using the NanoString (58, 59) Fibrosis Panel and a custom panel of bone-specific genes available through the UCSF Skeletal Biology and Biomechanics Core.

Silver Nitrate Staining. Femurs from male young (2 mo, $n = 3$) and aged (35 to 37 mo, $n = 5$) C57BL/6 mice (Buck Institute) and male young (2 mo) TβRII$^{ocy-/-}$ mice and their TβRII^{ctrl} littermates ($n = 4$ to 5 each) were prepared for histological examination via silver nitrate staining as described elsewhere (9, 49, 57) and two-dimensional (2D) canalicular length quantified utilizing Fiji/ImageJ (60).

Fluorescent Imaging of the LCN. Dissected femurs were fixed, demineralized, and prepared for cryosectioning and fluorescent imaging as previously described (11, 12, 57). Briefly, staining of the LCN was accomplished utilizing the hydrophobic lipophilic membrane dye DiI (Thermo Fisher), Alexa Fluor 488-Phalloidin to visualize the actin cytoskeleton (Thermo Fisher), and DAPI to identify cell nuclei. Bone sections were optically cleared and imaged on a Lecia DMi8 (Leica Microsystems) inverted confocal microscope running LAS X software.

Structural Analysis. Quantification of canalicular tortuosity, canalicular spacing, and the LCN volume fraction of the LCN in 3D was completed using a combination of Fiji plugins, including BoneJ (61) and the Simple Neurite Tracer. Imaris (Oxford Instruments), made available by the UCSF Biological Imaging and Development Core, was used to segment and quantify the canalicular sprouting points within the first bifurcation (S.1) and observe canalicular branching behavior in expanding concentric regions along canaliculi away from the cell body.

Connectomic Network Analysis. Connectomic network analysis of the LCN was accomplished on skeletonized representative maps of binarized, 8-bit confocal stacks of the LCN ($n = 5$ per group) as described in Kollmannsberger et al. (36). Connectomic measurements were completed utilizing the MATLAB (Mathworks) scripts provided from the Kollmannsberger et al. GitHub (62).* Updated scripts with custom MEX files and C+ wrappers were used to run scripts.(63)†

Finite Element Model Generation. Materialise Mimics image processing software was employed to generate a 3D model of the osteocytes from fluorescent confocal image stacks. Confocal image stacks of 20 ($n = 5$ per group) osteocytes were imported into Mimics and thresholded to allow segmentation of the osteocytes. Individual osteocytes were selected from deep within the bone tissue by selecting a ~25 × 25 × 25-μm region of interest around a single DAPI nuclear signal. To prevent loss of information during segmentation or inclusion of confounding local features, a minimum distance of 10 μm from the edge of the field of view and from large local landmarks (e.g., blood vessels) was ensured. Models were then meshed using 3-Matic voxel-meshing software (Materialise) as described previously (64). Models were dimensionally constrained so that no feature was thinner than the effective optical "diffraction limit" of the used flourophores (3 pixels/~450 nm) at any location. At sites where the dendritic dimensions are greater than ~450 nm in diameter, these measured dimensions were used in the mesh. Dimensions of the PCS based on previous experimental measurements (42, 53, 54) were used to model the interstitial fluid flow. This uniform 0.08-μm PCS offset was applied to the osteocyte mesh surface followed by a Boolean subtraction to remove the osteocyte volume. This offset was reduced and multiplied by a factor of two to create the constricted (0.04-μm) and expanded (0.16-μm) PCS models around the same base cellular geometry. Geometries were meshed using four-noded tetrahedral elements and exported to COMSOL multiphysics computational modeling software. Representative resultant 3D models of the three PCS conditions from confocal image-derived images are shown in Fig. 4*A*. Similar methods were used to mesh and model three individual canalicular channels per group.

Computational Fluid Dynamics. The properties of the interstitial fluid were assumed to be similar to salt water, with a density of 997 kg · m^{-3} and a dynamic viscosity of 0.000855 kg · m^{-1} · s^{-1} [48,63]. Flow within the lacunar-canalicular system was assumed to be laminar in nature. A pressure gradient was applied across the models to represent organ-level mechanical loading that generates regions of compression and tension driving fluid across the LCN (20, 65, 66). An inlet pressure of 300 Pa was assigned to the inlets on one face, and the remaining inlets were defined as outlets at a relative pressure of 0 Pa (20, 66), similar to the pressure gradient applied by Anderson et al. (65) Models with altered volumes of PCS resulted in altered flow rates under these consistently applied boundary assumptions. Interstitial fluid velocity and shear stress were recorded as the 95th percentile values.

*https://github.com/phi-max/OCY_connectomics.

†https://github.com/cschurm/ocy_connectomics_updated.

Statistical Analysis. A two-way ANOVA with multiple post hoc Tukey-corrected comparisons was completed on canalicular-length results from silver nitrate staining. In post hoc comparisons, pairwise comparisons between the control groups were nonsignificant as were comparisons between the degenerated models. The four remaining pairwise comparisons between each degenerated model to either control were highly significant ($P < 0.01$). All following statistical comparisons were made between each degenerated model and their proper control (2 mo WT versus 36 mo WT, $T\beta RII^{ctrl}$ versus $T\beta RII^{ocy-/-}$) utilizing a two-sided Student's *t* test with a defined alpha level of 0.05 (indicated by * in figures). Prism 8.4 (GraphPad Software, Inc.) was used for all statistical comparisons. Unless otherwise stated, data are presented as mean ± SD.

Data Availability. MATLAB code data have been deposited in the GitHub repository: https://github.com/cschurm/ocy_connectomics_updated. All other study data are included in the article and/or supporting information.

ACKNOWLEDGMENTS. This research was supported by NIH National Institute of Dental and Craniofacial Research Grant R01 DE019284 (T.A.) and NIH National Institute on Aging Grant F31 AG063402 (C.A.S.). This project also received funding from the European Union's Horizon 2020 research and innovation program under Marie Sklodowska-Curie Grant 748305 (S.W.V.). UCSF cores used to complete this work include the Skeletal Biology and Biomechanics Core of the Core Center for Musculoskeletal Biology and Medicine (NIH National Institute of Arthritis and Musculoskeletal and Skin Diseases Grant P30 AR066262) and the Biological Imaging and Development Core and staff for support using Imaris. The authors thank Dr. X. E. Guo for helpful discussions, the Guo Laboratory at Columbia University for computational resources (Mimics), Dr. R. Orendorff for software expertise and support with the MATLAB scripts, and Drs. S. Melov and J. Garrison at the Buck Institute for Research on Aging for donation of young and aged murine tissues.

1. H. Razi *et al*., Aging leads to a dysregulation in mechanically driven bone formation and resorption. *J. Bone Miner. Res.* **30**, 1864–1873 (2015).
2. M. Almeida, Aging mechanisms in bone. *Bonekey Rep.* **1**, 102 (2012).
3. P. R. Buenzli, N. A. Sims, Quantifying the osteocyte network in the human skeleton. *Bone* **75**, 144–150 (2015).
4. L. F. Bonewald, The amazing osteocyte. *J. Bone Miner. Res.* **26**, 229–238 (2011).
5. M. B. Schaffler, O. D. Kennedy, Osteocyte signaling in bone. *Curr. Osteoporos. Rep.* **10**, 118–125 (2012).
6. M. B. Schaffler, W.-Y. Cheung, R. Majeska, O. Kennedy, Osteocytes: Master orchestrators of bone. *Calcif. Tissue Int.* **94**, 5–24 (2014).
7. Y. Uda, E. Azab, N. Sun, C. Shi, P. D. Pajevic, Osteocyte mechanobiology. *Curr. Osteoporos. Rep.* **15**, 318–325 (2017).
8. N. Nango *et al*., Osteocyte-directed bone demineralization along canaliculi. *Bone* **84**, 279–288 (2016).
9. N. S. Dole *et al*., Osteocyte-intrinsic TGF-β signaling regulates bone quality through perilacunar/canalicular remodeling. *Cell Rep.* **21**, 2585–2596 (2017).
10. H. Qing *et al*., Demonstration of osteocytic perilacunar/canalicular remodeling in mice during lactation. *J. Bone Miner. Res.* **27**, 1018–1029 (2012).
11. L. M. Tiede-Lewis *et al*., Degeneration of the osteocyte network in the C57BL/6 mouse model of aging. *Aging (Albany NY)* **9**, 2190–2208 (2017).
12. S. A. Kamel-ElSayed, L. M. Tiede-Lewis, Y. Lu, P. A. Veno, S. L. Dallas, Novel approaches for two and three dimensional multiplexed imaging of osteocytes. *Bone* **76**, 129–140 (2015).
13. C. M. Heveran, A. Rauff, K. B. King, R. D. Carpenter, V. L. Ferguson, A new open-source tool for measuring 3D osteocyte lacunar geometries from confocal laser scanning microscopy reveals age-related changes to lacunar size and shape in cortical mouse bone. *Bone* **110**, 115–127 (2018).
14. L. B. Meakin, G. L. Galea, T. Sugiyama, L. E. Lanyon, J. S. Price, Age-related impairment of bones' adaptive response to loading in mice is associated with sex-related deficiencies in osteoblasts but no change in osteocytes. *J. Bone Miner. Res.* **29**, 1859–1871 (2014).
15. R. K. Nalla, J. J. Kruzic, J. H. Kinney, R. O. Ritchie, Effect of aging on the toughness of human cortical bone: Evaluation by R-curves. *Bone* **35**, 1240–1246 (2004).
16. E. A. Zimmermann *et al*., Age-related changes in the plasticity and toughness of human cortical bone at multiple length scales. *Proc. Natl. Acad. Sci. U.S.A.* **108**, 14416–14421 (2011).
17. L. M. Tiede-Lewis, S. L. Dallas, Changes in the osteocyte lacunocanalicular network with aging. *Bone* **122**, 101–113 (2019).
18. S. Weinbaum, S. C. Cowin, Y. Zeng, A model for the excitation of osteocytes by mechanical loading-induced bone fluid shear stresses. *J. Biomech.* **27**, 339–360 (1994).
19. S. W. Verbruggen, T. J. Vaughan, L. M. McNamara, Mechanisms of osteocyte stimulation in osteoporosis. *J. Mech. Behav. Biomed. Mater.* **62**, 158–168 (2016).
20. R. Steck, P. Niederer, M. L. Knothe Tate, A finite element analysis for the prediction of load-induced fluid flow and mechanochemical transduction in bone. *J. Theor. Biol.* **220**, 249–259 (2003).
21. T. Ganesh, L. E. Laughrey, M. Niroobakhsh, N. Lara-Castillo, Multiscale finite element modeling of mechanical strains and fluid flow in osteocyte lacunocanalicular system. *Bone* **137**, 115328 (2020).
22. M. J. Silva *et al*., Tibial loading increases osteogenic gene expression and cortical bone volume in mature and middle-aged mice. *PLoS One* **7**, e34980 (2012).
23. C. J. Chermside-Scabbo *et al*. Old mice have less transcriptional activation but similar periosteal cell proliferation compared to young-adult mice in response to in vivo mechanical loading. *J. Bone Miner. Res.* **35**, 1751–1764 (2020).
24. N. Holguin, M. D. Brodt, M. E. Sanchez, M. J. Silva, Aging diminishes lamellar and woven bone formation induced by tibial compression in adult C57BL/6. *Bone* **65**, 83–91 (2014).
25. M. Kerschnitzki *et al*., Architecture of the osteocyte network correlates with bone material quality. *J. Bone Miner. Res.* **28**, 1837–1845 (2013).
26. W. T. George, D. Vashishth, Susceptibility of aging human bone to mixed-mode fracture increases bone fragility. *Bone* **38**, 105–111 (2006).
27. D. B. Burr, Changes in bone matrix properties with aging. *Bone* **120**, 85–93 (2019).
28. S. A. Wainwright *et al*.; Study of Osteoporotic Fractures Research Group, Hip fracture in women without osteoporosis. *J. Clin. Endocrinol. Metab.* **90**, 2787–2793 (2005).
29. C. M. Heveran *et al*., Chronic kidney disease and aging differentially diminish bone material and microarchitecture in C57Bl/6 mice. *Bone* **127**, 91–103 (2019).
30. S. A. Colopy *et al*., Response of the osteocyte syncytium adjacent to and distant from linear microcracks during adaptation to cyclic fatigue loading. *Bone* **35**, 881–891 (2004).
31. J. Nguyen, S. Y. Tang, D. Nguyen, T. Alliston, Load regulates bone formation and sclerostin expression through a TGFβ-dependent mechanism. *PLoS One* **8**, e53813 (2013).
32. S. Y. Tang, R. P. Herber, S. P. Ho, T. Alliston, Matrix metalloproteinase-13 is required for osteocytic perilacunar remodeling and maintains bone fracture resistance. *J. Bone Miner. Res.* **27**, 1936–1950 (2012).
33. I. Grafe *et al*., Excessive transforming growth factor-β signaling is a common mechanism in osteogenesis imperfecta. *Nat. Med.* **20**, 670–675 (2014).
34. K. Janssens, P. ten Dijke, S. H. Ralston, C. Bergmann, W. Van Hul, Transforming growth factor-beta 1 mutations in Camurati-Engelmann disease lead to increased signaling by altering either activation or secretion of the mutant protein. *J. Biol. Chem.* **278**, 7718–7724 (2003).
35. S. L. Dallas, T. Alliston, L. F. Bonewald, "Chapter 53 - Transforming Growth Factor-β" in *Principles of Bone Biology*, J. P. Bilezikian, L. G. Raisz, T. J. Martin, Eds. (Academic Press, ed. 3, 2008), pp. 1145–1166.
36. P. Kollmannsberger *et al*., The small world of osteocytes: Connectomics of the lacuno-canalicular network in bone. *New J. Phys.* **19**, 073019 (2017).
37. R. Weinkamer, P. Kollmannsberger, P. Fratzl, Towards a connectomic description of the osteocyte lacunocanalicular network in bone. *Curr. Osteoporos. Rep.* **17**, 186–194 (2019).
38. N. K. Wittig *et al*., Canalicular junctions in the osteocyte lacuno-canalicular network of cortical bone. *ACS Nano* **13**, 6421–6430 (2019).
39. X. Lai *et al*., The dependences of osteocyte network on bone compartment, age, and disease. *Bone Res.* **3**, E318 (2015).
40. B. Hesse *et al*., Canalicular network morphology is the major determinant of the spatial distribution of mass density in human bone tissue: Evidence by means of synchrotron radiation phase-contrast nano-CT. *J. Bone Miner. Res.* **30**, 346–356 (2015).
41. L. Wang, C. Ciani, S. B. Doty, S. P. Fritton, Delineating bone's interstitial fluid pathway in vivo. *Bone* **34**, 499–509 (2004).
42. L. Wang *et al*., In situ measurement of solute transport in the bone lacunar-canalicular system. *Proc. Natl. Acad. Sci. U.S.A.* **102**, 11911–11916 (2005).
43. A. R. Wijenayaka *et al*., Sclerostin stimulates osteocyte support of osteoclast activity by a RANKL-dependent pathway. *PLoS One* **6**, e25900 (2011).
44. V. Gatti, E. M. Azoulay, S. P. Fritton, Microstructural changes associated with osteoporosis negatively affect loading-induced fluid flow around osteocytes in cortical bone. *J. Biomech.* **66**, 127–136 (2018).
45. Y. Han, S. C. Cowin, M. B. Schaffler, S. Weinbaum, Mechanotransduction and strain amplification in osteocyte cell processes. *Proc. Natl. Acad. Sci. U.S.A.* **101**, 16689–16694 (2004).
46. E. J. Anderson, M. L. Knothe Tate, Idealization of pericellular fluid space geometry and dimension results in a profound underprediction of nano-microscale stresses imparted by fluid drag on osteocytes. *J. Biomech.* **41**, 1736–1746 (2008).
47. H. Kamioka *et al*., Microscale fluid flow analysis in a human osteocyte canaliculus using a realistic high-resolution image-based three-dimensional model. *Integr. Biol.* **4**, 1198–1206 (2012).
48. S. W. Verbruggen, T. J. Vaughan, L. M. McNamara, Fluid flow in the osteocyte mechanical environment: A fluid-structure interaction approach. *Biomech. Model. Mechanobiol.* **13**, 85–97 (2014).
49. C. S. Yee, C. A. Schurman, C. R. White, T. Alliston, Investigating osteocytic perilacunar/canalicular remodeling. *Curr. Osteoporos. Rep.* **17**, 157–168 (2019).
50. S. W. Verbruggen, M. J. Mc Garrigle, M. G. Haugh, M. C. Voisin, L. M. McNamara, Altered mechanical environment of bone cells in an animal model of short- and long-term osteoporosis. *Biophys. J.* **108**, 1587–1598 (2015).
51. T. Adachi *et al*., Calcium response in single osteocytes to locally applied mechanical stimulus: Differences in cell process and cell body. *J. Biomech.* **42**, 1989–1995 (2009).
52. S. Burra *et al*., Dendritic processes of osteocytes are mechanotransducers that induce the opening of hemichannels. *Proc. Natl. Acad. Sci. U.S.A.* **107**, 13648–13653 (2010).
53. L. M. McNamara, R. J. Majeska, S. Weinbaum, V. Friedrich, M. B. Schaffler, Attachment of osteocyte cell processes to the bone matrix. *Anat. Rec. (Hoboken)* **292**, 355–363 (2009).
54. L.-D. You, S. Weinbaum, S. C. Cowin, M. B. Schaffler, Ultrastructure of the osteocyte process and its pericellular matrix. *Anat. Rec. A Discov. Mol. Cell. Evol. Biol.* **278**, 505–513 (2004).

55. S. Kaya *et al*., Lactation-induced changes in the volume of osteocyte lacunar-canalicular space alter mechanical properties in cortical bone tissue. *J. Bone Miner. Res.* **32**, 688–697 (2017).
56. Y. Tang *et al*., MT1-MMP-dependent control of skeletal stem cell commitment via a β1-integrin/YAP/TAZ signaling axis. *Dev. Cell* **25**, 402–416 (2013).
57. N. S. Dole, C. S. Yee, C. A. Schurman, S. L. Dallas, T. Alliston, Assessment of osteocytes: Techniques for studying morphological and molecular changes associated with peri-lacunar/canalicular remodeling of the bone matrix. *Methods Mol. Biol.* **2230**, 303–323 (2021).
58. M. H. Veldman-Jones *et al*., Evaluating robustness and sensitivity of the NanoString Technologies nCounter platform to enable multiplexed gene expression analysis of clinical samples. *Cancer Res.* **75**, 2587–2593 (2015).
59. G. K. Geiss *et al*., Direct multiplexed measurement of gene expression with color-coded probe pairs. *Nat. Biotechnol.* **26**, 317–325 (2008).
60. J. Schindelin *et al*., Fiji: An open-source platform for biological-image analysis. *Nat. Methods* **9**, 676–682 (2012).
61. M. Doube *et al*., BoneJ: Free and extensible bone image analysis in ImageJ. *Bone* **47**, 1076–1079 (2010).
62. P. Kollmannsberger, OCY_connectomics. GitHub. https://github.com/phi-max/OCY_connectomics. Deposited 14 February 2017.
63. C.A. Schurman, R. Orendorff, ocy_connectomics_updated. GitHub. https://github.com/cschurm/ocy_connectomics_updated. Deposited 18 August 2020.
64. S. W. Verbruggen, T. J. Vaughan, L. M. McNamara, Strain amplification in bone mechanobiology: A computational investigation of the in vivo mechanics of osteocytes. *J. R. Soc. Interface* **9**, 2735–2744 (2012).
65. E. J. Anderson, S. Kaliyamoorthy, J. Iwan, D. Alexander, M. L. Knothe Tate, Nano-microscale models of periosteocytic flow show differences in stresses imparted to cell body and processes. *Ann. Biomed. Eng.* **33**, 52–62 (2005).
66. P. Manfredini, G. Cocchetti, G. Maier, A. Redaelli, F. M. Montevecchi, Poroelastic finite element analysis of a bone specimen under cyclic loading. *J. Biomech.* **32**, 135–144 (1999).